# Supplementary Material for Perturbing open cavities: Anomalous resonance frequency shifts in a hybrid cavity-nanoantenna system

Freek Ruesink,[1] Hugo M. Doeleman,[1,2] Ruud Hendrikx,[1] A. Femius Koenderink,[1,2] and Ewold Verhagen[1]

[1]*FOM Institute AMOLF, Science Park 104, 1098 XG, Amsterdam, The Netherlands*
[2]*Institute of Physics, University of Amsterdam, P.O. Box 94485, 1090 GL Amsterdam, The Netherlands*

## CONTENTS

# I. BETHE-SCHWINGER CAVITY PERTURBATION IN OPEN SYSTEMS

In this section, we show the derivation of the Bethe-Schwinger cavity perturbation formula, analogous to the approach by [1, 2]. Afterwards, we discuss how small approximations result in equation (1) of the main text. We note, that the calculation of the different contributions to the eigenfrequency change in our simulations did not involve the approximated equation (1), but the formula as shown in equation (S16).

## A. Eigenmodes

We consider the modes of an open cavity described by a spatial distribution of permittivity $\epsilon_0\epsilon(\mathbf{r})$ and permeability $\mu_0\mu(\mathbf{r})$ (in the following, the spatial dependence of both is implicitly assumed). The eigenmodes of the system are found by solving Maxwell's equations in all of space in the absence of external drives. This yields solutions of the form

$$\mathbf{E}(\mathbf{r}, t) = \mathbf{E}_0(\mathbf{r})e^{-i\omega t}, \tag{S1}$$
$$\mathbf{H}(\mathbf{r}, t) = \mathbf{H}_0(\mathbf{r})e^{-i\omega t}, \tag{S2}$$

which satisfy Maxwell's equations for some complex frequency

$$\omega = \omega_c - i\frac{\kappa}{2}, \tag{S3}$$

where $\omega_c$ and $\kappa$ denote the (real) resonance frequency and energy decay rate, respectively. Typically, we will consider systems where $\kappa \ll \omega_c$, such that $\omega \approx \omega^*$. Important relationships between $\mathbf{E}_0$ and $\mathbf{H}_0$ now include

$$\nabla \times \mathbf{E}_0 = i\omega\mu_0\mu\mathbf{H}_0 \qquad \nabla \times \mathbf{E}_0^* = -i\omega\mu_0\mu\mathbf{H}_0^*, \tag{S4}$$
$$\nabla \times \mathbf{H}_0 = -i\omega\epsilon_0\epsilon\mathbf{E}_0 \qquad \nabla \times \mathbf{H}_0^* = i\omega\epsilon_0\epsilon\mathbf{E}_0^*. \tag{S5}$$

## B. Dielectric perturbation

We now consider that the cavity is perturbed, such that in a finite volume $\Delta V$, the relative permittivity and permeability are changed to new values

$$\epsilon_p = \epsilon + \Delta\epsilon, \tag{S6}$$
$$\mu_p = \mu + \Delta\mu. \tag{S7}$$

This perturbed system has different eigenmodes written as

$$\mathbf{E}(\mathbf{r}, t) = \mathbf{E}_p(\mathbf{r})e^{-i\omega_p t} = (\mathbf{E}_0(\mathbf{r}) + \delta\mathbf{E}(\mathbf{r})) e^{-i(\omega+\delta\omega)t}, \tag{S8}$$
$$\mathbf{H}(\mathbf{r}, t) = \mathbf{H}_p(\mathbf{r})e^{-i\omega_p t} = (\mathbf{H}_0(\mathbf{r}) + \delta\mathbf{H}(\mathbf{r})) e^{-i(\omega+\delta\omega)t}, \tag{S9}$$

where $\mathbf{E}_p(\mathbf{r})$ and $\omega_p$ describe the spatial dependence and resonance frequency of the perturbed cavity mode. Defining $\delta\mathbf{E} = \mathbf{E}_p - \mathbf{E}_0$, $\delta\mathbf{H} = \mathbf{H}_p - \mathbf{H}_0$ and $\delta\omega = \omega_p - \omega$ yields

$$\nabla \times (\mathbf{E}_0 + \delta\mathbf{E}) = i(\omega + \delta\omega)\mu_0\mu_p(\mathbf{H}_0 + \delta\mathbf{H}), \tag{S10}$$
$$\nabla \times (\mathbf{H}_0 + \delta\mathbf{H}) = -i(\omega + \delta\omega)\epsilon_0\epsilon_p(\mathbf{E}_0 + \delta\mathbf{E}). \tag{S11}$$

Combining the above equations for the curl of the fields gives

$$\nabla \times \delta\mathbf{E} = i\omega_p\mu_0\mu_p\mathbf{H}_p - i\omega\mu_0\mu\mathbf{H}_0, \tag{S12}$$
$$\nabla \times \delta\mathbf{H} = -i\omega_p\epsilon_0\epsilon_p\mathbf{E}_p + i\omega\epsilon_0\epsilon\mathbf{E}_0. \tag{S13}$$

We next take the dot product of $\mathbf{H}_0^*$ and $\mathbf{E}_0^*$ with the curls of $\delta\mathbf{E}$ and $\delta\mathbf{H}$, respectively and rewrite both making use of the vector identity

$$\mathbf{a} \cdot (\nabla \times \mathbf{b}) = \mathbf{b} \cdot (\nabla \times \mathbf{a}) - \nabla \cdot (\mathbf{a} \times \mathbf{b}). \tag{S14}$$

Subtracting the obtained expressions gives us

$$\delta\omega \left(\epsilon_0\epsilon\mathbf{E}_0^* \cdot \mathbf{E}_p + \mu_0\mu\mathbf{H}_0^* \cdot \mathbf{H}_p\right) = -\left(\omega + \delta\omega\right)\left(\epsilon_0\Delta\epsilon\mathbf{E}_0^* \cdot \mathbf{E}_p + \mu_0\Delta\mu\mathbf{H}_0^* \cdot \mathbf{H}_p\right)$$
$$- i\left(\nabla \cdot (\delta\mathbf{E} \times \mathbf{H}_0^*) + \nabla \cdot (\mathbf{E}_0^* \times \delta\mathbf{H})\right). \tag{S15}$$

Finally, we take the integral of both sides over a (very large) volume $V$, and apply Gauss's theorem to arrive at the *Bethe-Schwinger equation* [3]:

$$\delta\omega \int_V dV \left[\epsilon_0\epsilon\mathbf{E}_0^* \cdot \mathbf{E}_p + \mu_0\mu\mathbf{H}_0^* \cdot \mathbf{H}_p\right] = -\left(\omega + \delta\omega\right) \int_{\Delta V} dV \left[\epsilon_0\Delta\epsilon\mathbf{E}_0^* \cdot \mathbf{E}_p + \mu_0\Delta\mu\mathbf{H}_0^* \cdot \mathbf{H}_p\right]$$

$$-\,\mathrm{i}\int_{\partial V} dA \left[(\delta\mathbf{E} \times \mathbf{H}_0^*) \cdot \hat{\mathbf{n}} + (\mathbf{E}_0^* \times \delta\mathbf{H}) \cdot \hat{\mathbf{n}}\right], \qquad (S16)$$

where $\partial V$ denotes the boundary of $V$ and $\hat{\mathbf{n}}$ the unit vector normal to that surface.

### C. Approximating the cavity perturbation

The above equation (S16) yields an expression for the (complex) cavity shift

$$\delta\omega = \delta\omega_{\mathrm{c}} - \mathrm{i}\frac{\delta\kappa}{2}. \qquad (S17)$$

To arrive at equation (1) of the main paper, we start by making the following approximations: If the effect of the perturbation is small, then $\omega + \delta\omega \approx \omega$, and when the total volume is large compared to the volume of the perturbation, it will be allowed to omit the contribution of $\mathbf{E}_0^* \cdot \delta\mathbf{E}$ in the integral on the left side of equation (S16), which can now be written as

$$\delta\omega \int_V dV \left[\epsilon_0\epsilon\mathbf{E}_0^* \cdot \mathbf{E}_p + \mu_0\mu\mathbf{H}_0^* \cdot \mathbf{H}_p\right] \approx \delta\omega \int_V dV \left[\epsilon_0\epsilon\left|\mathbf{E}_0\right|^2 + \mu_0\mu\left|\mathbf{H}_0\right|^2\right] = 4\delta\omega U_0,$$

where $U_0$ denotes the energy stored in the unperturbed cavity. Now the Bethe-Schwinger equation becomes

$$\delta\omega = -\frac{\omega}{4U_0}\int_{\Delta V} dV \left[\epsilon_0\Delta\epsilon\mathbf{E}_0^* \cdot \mathbf{E}_p + \mu_0\Delta\mu\mathbf{H}_0^* \cdot \mathbf{H}_p\right] - \frac{\mathrm{i}}{4U_0}\int_{\partial V} dA \left[(\delta\mathbf{E} \times \mathbf{H}_0^*) \cdot \hat{\mathbf{n}} + (\mathbf{E}_0^* \times \delta\mathbf{H}) \cdot \hat{\mathbf{n}}\right]. \qquad (S18)$$

If the perturbation is caused by a variation of the permittivity ($\Delta\mu = 0$) and if the dimensions of its volume $\Delta V$ are small compared to the scale over which the cavity field $\mathbf{E}_0$ varies, one can make a useful approximation by considering the perturbation as a polarizable (point) dipole. Its total dipole moment $\mathbf{p}$ is given by

$$\mathbf{p} = \int_{\Delta V} \mathrm{d}V \frac{\mathrm{d}\mathbf{p}}{\mathrm{d}V}, \qquad (S19)$$

where we introduced the dipole moment per unit volume, which we identify as

$$\frac{\mathrm{d}\mathbf{p}}{\mathrm{d}V}(\mathbf{r}) = \epsilon_0\left(\epsilon_p - \epsilon\right)\mathbf{E}_p(\mathbf{r}) = \epsilon_0\Delta\epsilon\mathbf{E}_p(\mathbf{r}). \qquad (S20)$$

Taking into account that $\mathbf{E}_0$ can be considered constant over $\Delta V$, we can now write the integral over $\Delta V$ in equation (S18) as

$$\mathbf{E}_0^* \cdot \epsilon_0 \int_{\Delta V} \mathrm{d}V\Delta\epsilon\mathbf{E}_p = \mathbf{E}_0^* \cdot \mathbf{p} = \mathbf{E}_0^* \cdot \overset{\leftrightarrow}{\alpha}\,\mathbf{E}_0, \qquad (S21)$$

where we have introduced the polarizability $\overset{\leftrightarrow}{\alpha}$ defined in this case through

$$\mathbf{p} = \overset{\leftrightarrow}{\alpha}\,\mathbf{E}_0. \qquad (S22)$$

If $\overset{\leftrightarrow}{\alpha}$ is diagonal, and we denote the magnitude of the polarizability in the direction of the cavity field by the scalar $\alpha$, the integral over $\Delta V$ reduces to $\alpha\left|\mathbf{E}_0\right|^2$. In this approach, we arrive at a new version of the Bethe-Schwinger equation for the perturbation of the cavity frequency:

$$\delta\omega = -\omega\frac{\alpha\left|\mathbf{E}_0\right|^2}{4U_0} - \frac{\mathrm{i}}{4U_0}\int_{\partial V} dA \left[(\delta\mathbf{E} \times \mathbf{H}_0^*) \cdot \hat{\mathbf{n}} + (\mathbf{E}_0^* \times \delta\mathbf{H}) \cdot \hat{\mathbf{n}}\right], \qquad (S23)$$

Here we see how the real part of the particle's polarizability contributes to a frequency shift of the cavity, but so does the imaginary part of the surface integral. Likewise, the change of the cavity linewidth is related to the imaginary part of $\alpha$ and the real part of the integral over $\partial V$.
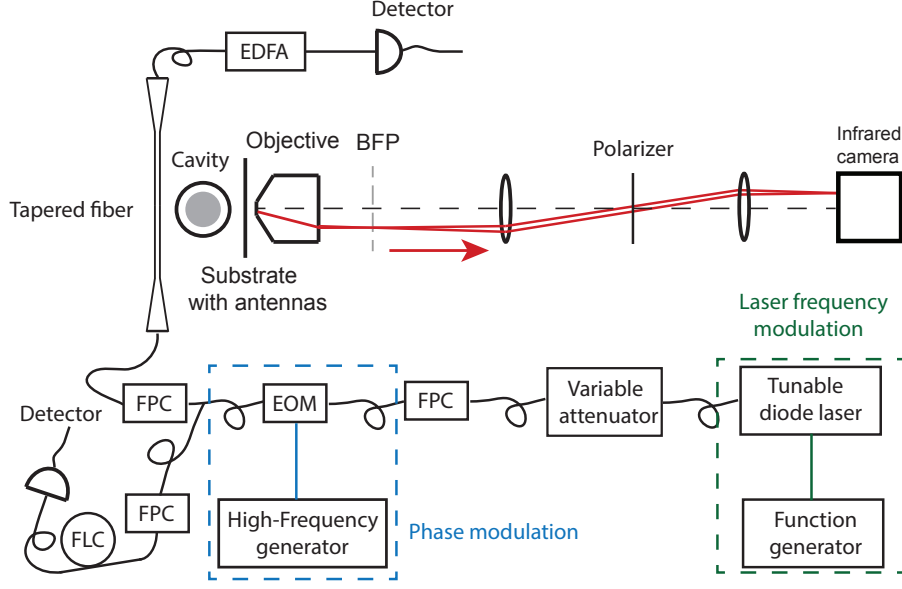
FIG. S1. **Experimental setup.** See text for details.

## II. EXPERIMENTAL DETAILS

### A. Sample fabrication

Gold nanoantennas are fabricated in an array on a 170 $\mu$m thick glass coverslide. To start, a 130 nm layer of ZEP-520 resist is spin-coated on top of the coverslide. The nanoantennas are patterned into the resist using electron-beam lithography. After development, thermal evaporation of gold and a lift-off step yield the desired antennas. The antenna width and thickness were designed to be 120 and 40 nm and the length was varied between 400 and 360 nm. The pitch along the short-axes of the antennas was varied between 750 and 1500 nm, and the pitch along the long-axes was fixed at 800 nm. A high-Q silica microtoroid (diameter $\approx 36$ $\mu$m) is fabricated on the edge of a silicon sample, largely following methods as previously reported [4, 5]. In this work, spin-coating (ma-N 2410) and subsequent cleaving of the sample enabled targeted e-beam lithography of the disks.

### B. Experimental Setup

Figure S1 shows the experimental setup used in this work. We use a tunable fiber-coupled external cavity diode laser (New Focus TLB-6728, <100 kHz linewidth) to probe the microcavity. The laser frequency is controlled by an external voltage from a function generator. Coupling of light into the cavity is achieved using a tapered optical fiber, of which the position is controlled using piezo positioners (not shown). The electro-optical modulator (EOM, EOspace) is used to generate sidebands of the cavity mode at known RF frequency, which allows for calibration of our optical frequency axis. Fiber polarization controllers (FPC) ensure effective coupling into the optical cavity mode of interest. Before detection, the light that is transmitted through the tapered fiber is amplified using an Erbium Doped Fiber Amplifier (EDFA). Radiation leakage from the microcavity is collected using an objective (Nikon, CFI Apo TIRF 100x) to obtain information regarding polarization and mode profile (through fourier-space imaging and polarization analysis of the back focal plane (BFP), Fig. S2) of the cavity mode. Using this method we identify a fundamental cavity mode, of which the polarization is aligned with the long axes of the antennas. Due to limitations with regards to the numerical aperture (NA) of our objective (NA $\approx 1.33$), imaging of the complete cavity mode-profile is impossible, thus resulting in a cut-off of the imaged mode profile. Considering this cut-off at NA=1.33 and the refractive index of silica (1.46), we estimate an effective mode index of around 1.35. We check the frequency stability of the laser itself using a fiber loop reference cavity (FLC).
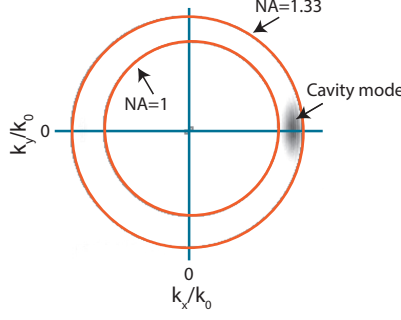
FIG. S2. **Mode characterization.** Illumination of the BFP of our objective with white light (not shown) is used to calibrate the image on our infrared camera. This involves fitting the NA = 1 ring and maximum collection angle of our objective (orange circles), which are imaged on the camera. Sample tilt results in a slight offset between the outer and NA=1 ring. Subsequent monitoring of the radiation leakage of our cavity mode enables its characterization (fundamental TE mode) and an estimate (see text) of the effective mode index ($\approx 1.35$). The blue solid lines serve as a guide to the eye.
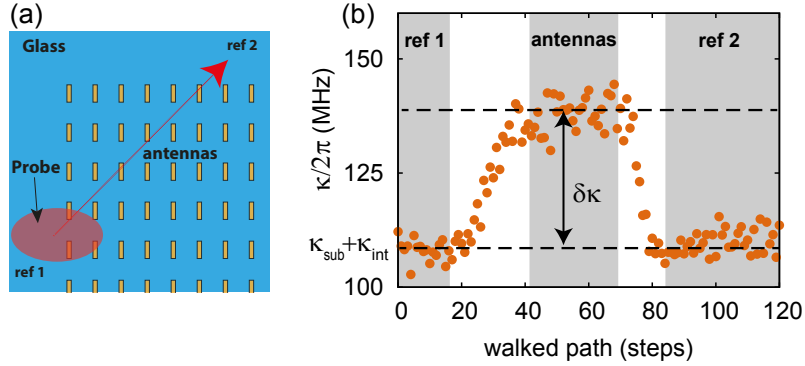


FIG. S3. **Scanning along an array.** a) Cartoon of a scan of the microcavity along the antenna array. Careful alignment allows us to scan over the antennas by moving our microcavity between two predefined points (ref 1 and ref 2), which serve as our reference measurements on glass. Between those points we measure the effect of the antennas on the cavity mode. b) Evolution of the cavity linewidth during a scan along the antenna array, where each point is retrieved from a fit with a Lorentzian lineshape. When scanning along the antennas, we make sure that we see a *plateau* of data points. In our analysis, we only include the data points indicated by the grey regions, thus excluding the data taken during transit between reference and antennas. For the calculation of $\delta\kappa$, we average all the points clearly on the *plateau* and subtract the average reference value on glass ($\kappa_{\mathrm{ref}} = \kappa_{\mathrm{sub}} + \kappa_{\mathrm{int}}$).

## C. Measurement procedure

Figure S3a shows that the experimental data is obtained by stepwise scanning the microcavity, which is placed on a piezo-electric stage, along an antenna array and a stretch of bare substrate at a distance of $\sim 1.1$ $\mu$m (based on simulations). During each scan, the cavity-fiber distance is kept constant, which is checked before and after each experiment when the cavity is positioned at opposite positions adjacent to the antenna arrays. This check is performed by monitoring the cavity linewidth (broadened by the presence of the substrate), which depends strongly on the distance to the substrate. Each scan consists of 80-120 steps and multiple scans (2-5) are performed on each array. The change in resonance frequency ($\delta\omega_{\mathrm{c}}$) and linewidth ($\delta\kappa$) due to the antennas is obtained by subtracting the cavity resonance frequency and linewidth without the array placed in the near-field of the cavity, from the cavity resonance frequency and linewidth with the antenna array placed in the evanescent field of the cavity mode. Example data for the change in linewidth is shown in Fig. S3b. To correct for any remaining sample tilt and/or slow drift, reference measurements on glass taken at the start and end of a scan are averaged. The values of $\delta\omega_{\mathrm{c}}$ and $\delta\kappa$ are calculated by excluding data points taken during the transition from glass to array.

Even though we check that all measurements are performed at the same cavity-sample distance, we would like to eliminate any errors due to small variations of that distance. To this end, we retrieve parameters that are robust towards small distance changes by considering the relative change in linewidth(resonance frequency) due to the antennas: $\delta\kappa(\delta\omega_{\mathrm{c}})/\kappa_{\mathrm{sub}}$, where $\kappa_{\mathrm{sub}}$ is the broadening the cavity mode experiences due to the glass substrate ($\kappa_{\mathrm{sub}} =$
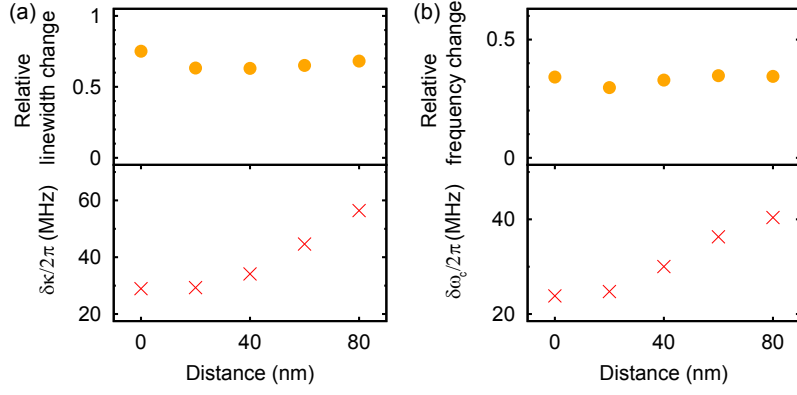
FIG. S4. **Validation of dimensionless parameter.** The measured effect on the cavity linewidth (a, bottom) and resonance frequency (b, bottom) due to the antennas is clearly increasing when the cavity travels a certain distance towards the antennas. As shown in the top panel of (a) and (b), our analysis results in a constant dimensionless quantity for the change in linewidth and frequency which does not depend on the distance to the antenna array.

$\kappa_{\mathrm{ref}} - \kappa_{\mathrm{int}}$, with $\kappa_{\mathrm{int}}$ the decay rate of the bare cavity). Figure S4 shows that this method results in a relative change of the resonance frequency $\omega_{\mathrm{c}}$ and linewidth $\kappa$ which is independent of the distance to the substrate. It is obvious that this quantity now allows straightforward averaging over multiple scans on the same array and comparison between different antenna arrays. Errors on the mean are calculated for $\delta\omega_{\mathrm{c}}$ and $\delta\kappa$, while the error (one standard deviation) on $\omega_a$ (and thus the detuning) is retrieved from a Gaussian fit to the sum of squared residuals, obtained by displacing the fit result with respect to the normal-incidence tranmission spectra of the antenna arrays.

## III.  FINITE-ELEMENT SIMULATIONS

To gain more insight in our experimental results, and to calculate the different contributions to the complex frequency shift $\delta\omega$, we perform 2D eigenfrequency simulations using the COMSOL software package (v5.0). The cavity (diameter $= 36$ $\mu$m) has a refractive index of 1.35, comparable to the experimentally determined effective index of our cavity mode and is placed 1.1 $\mu$m from the substrate, which has a refractive index of 1.5. The antenna is assigned a varying permittivity to mimic a change in detuning between cavity and antenna and for the surrounding we take a refractive index of 1. The simulation includes the use of a Perfectly Matched Layer (PML).

In our experiment, changing the length of the antennas results in a changing plasmon resonance, in turn causing a varying detuning between cavity and antenna resonance frequency. To mimic this in our simulation, we assign a tunable permitivitty, which has a Lorentzian lineshape, to the perturbing antenna(s):

$$\epsilon_p = 1 - \frac{\mathrm{S} * \gamma_{\mathrm{s}}/2}{\Delta_{\mathrm{s}} - \mathrm{i}\gamma_{\mathrm{s}}/2} \tag{S24}$$

Sweeping the variable $\Delta_{\mathrm{s}}$ now allows to calculate the change in cavity eigenfrequency as a function of detuning. The parameter S can be used to control the scattering strength of the antenna, while the antenna linewidth is held fixed at $\gamma_{\mathrm{s}} = 1$. To determine a sensible value of S, we analyze the eigenfrequency shift of the cavity when perturbed by 11 antennas (pitch 1500, Fig. S5a) for different values of S and choose a value (S=340) which yields the best resemblance to our experiment (Fig. S5b). The values for the relative change in linewidth and resonance frequency are obtained via similar analysis as performed in the experimental situation, thus involving separate simulations for the bare cavity, and cavity perturbed by just a glass substrate.

It is important to realize that the values $\Delta_{\mathrm{s}}$ and $\gamma_{\mathrm{s}}$ are input parameters in the simulation, which do not include the effect of radiation losses on the antenna linewidth and resonance frequency [6]. To allow for a fair comparison with our experiment, we fit the results retrieved from the simulation with a Fano lineshape (black lines in Fig. S5a), to obtain the radiation corrected values $\Delta$ and $\gamma$. Using these corrected values of $\Delta$ and $\gamma$, we rescale our horizontal axis and obtain Fig. S5b. Note that this approach resembles the experimental situation, where the radiation corrected values of $\Delta$ and $\gamma$ are retrieved from the normal-incidence transmission spectra. It can be observed from Fig. S5b that the orange (resonance frequency) and pink (linewidth) circles are a good, but not perfect, match to the experimentally obtained cavity frequency and linewidth change (blue circles). We attribute the discrepancy to the intrinsic difference between a 2D simulation, where the cavity is modeled as an infinite cylinder, and the experimental situation, which employs
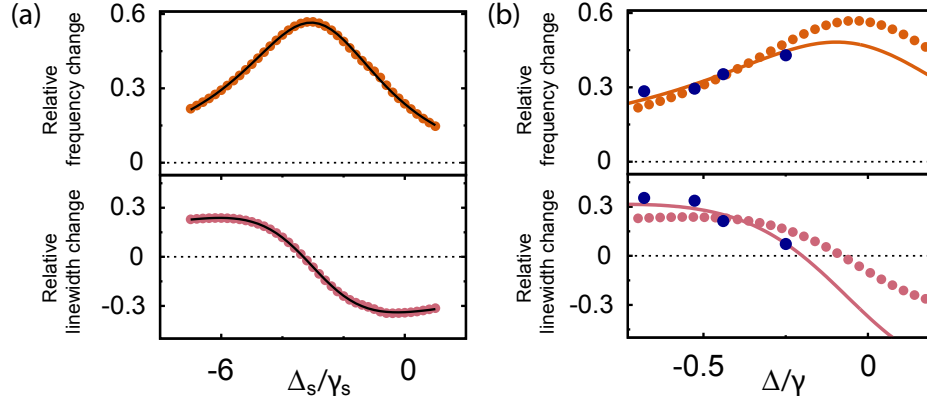
FIG. S5. **Using multiple scatterers to find the scattering strength S.** a) Filled circles: change in resonance frequency (top) and linewidth (bottom) of the cavity when perturbed by 11 antennas. The values on the horizontal axis are the input parameters in the simulation, which do not include effects due to radiation losses. Performing a fit (black line) using a fano-lineshape allows us to obtain the corrected values $\Delta$ and $\gamma$, which are used in (b). b) The blue circles and solid lines are experimental data points and a fit using the coupled-mode model, respectively. The orange (top) and pink (bottom) filled circles are the relative frequency and linewidth change that are obtained from a simulation with S=340. The rescaled horizontal axis is obtained from the fit in (a).

a toroidal cavity. This will necessarily change the radiation profile determining overlap and phase. Nonetheless, the 2D simulation reproduces all the main features observed in the experiment.

### A. Cavity and perturbation without glass

When calculating the complete Bethe-Schwinger formula, it is useful to first consider the situation where a cavity is perturbed by a single perturbing particle, in the absence of a substrate, as this should not allow for radiation interaction taking place, and thus result in a perturbation of the cavity eigenfrequency which is solely governed by the polarizability of the perturbing particle. The results of this simulation are shown in Fig. S6a. It is clear that the cavity indeed lacks radiation interaction (green stars) with the antenna and experiences linewidth and resonance frequency shifts that are solely related to the polarizability of the particle (black crosses), such that the total eigenfrequency change (open blue circles) is completely dominated by local effects. We remark that the Bethe-Schwinger cavity perturbation formula, which needs fields as it input, perfectly reproduces the cavity eigenfrequency shifts as predicted by the eigenvalues (orange(pink) filled circles) directly obtained from COMSOL.

### B. Cavity and perturbation with glass

As discussed in the main text, introducing a glass substrate enables and extra coupling channel between antenna and cavity due to overlapping radiation profiles. Fig. S6 shows results quantifying this effect for a cavity perturbed by a single antenna. Here the radiative interactions (green stars) are of importance when calculating the total (open blue circles) eigenfrequency shift of the cavity using the Bethe-Schwinger equation, dominating the effect of local perturbation (black crosses). Note that the calculation of complex $\delta\omega$ using the full Bethe Schwinger equation, yields almost exactly the same results when compared to the cavity eigenfrequency changes based on the eigenvalues calculated in the simulation (orange(frequency) and pink(linewidth) filled circles). We attribute the small difference that is observed mostly to the way joined data sets are handled in COMSOL. The use of joined datasets is necessary to obtain the fields $\delta\mathbf{E}$, but causes an error when integrating the closed-surface flux integrals (last terms of equation (1)). The reason is that for joined datasets COMSOL projects full datasets on a less dense intermediate mesh [7]. We performed mesh convergence studies to see if this effect would diminish with increasing mesh density (up to 60 elements/$\lambda_0$). Although we observe that both the eigenvalues and the fields of our solutions are clearly converged, the small difference in the cavity eigenfrequency shift that we obtain using both methods does not disappear. Nonetheless, the discrepancy is small enough to reproduce all observed trends.
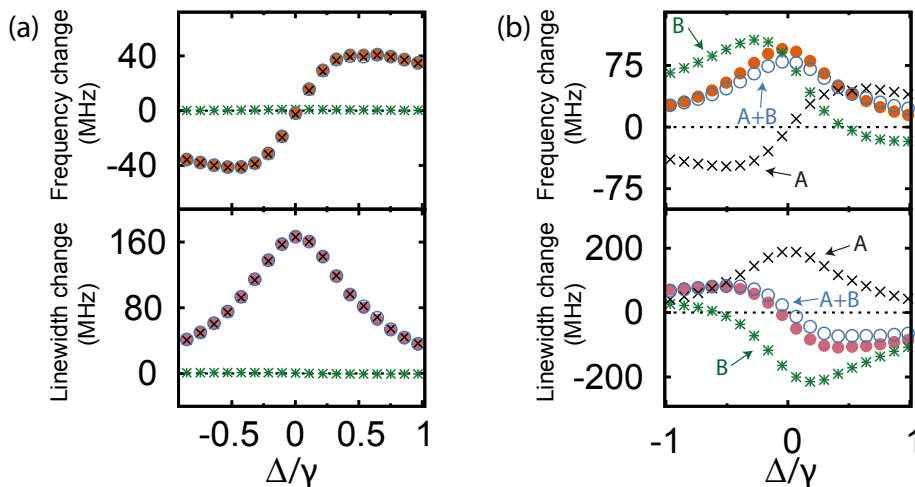
FIG. S6. **Benchmarking the calculation.** a) In the absence of a substrate, the cavity experiences a change in resonance frequency (top) and linewidth (bottom) that is solely associated with the polarizability (black crosses) of the perturbing particle, such that that the total eigenfrequency change as calculated by the Bethe-Schwinger equation (open blue circles) is completely dominated by local effects, leaving the radiative interaction (green stars) to be negligible. As expected, the Bethe-Schwinger cavity perturbation formula is able to perfectly reproduce the cavity eigenfrequency shifts when compared to the shifts obtained using the eigenvalues (orange(pink) filled circles) calculated by COMSOL b) In the situation where the substrate is present, as discussed in the main text, radiative interactions (green stars, A) are of importance when calculating the total (open blue circles, A+B) eigenfrequency shift of the cavity using the Bethe-Schwinger equation, dominating the local effect of the perturbation (black crosses, B). Note that the calculation of the full Bethe Schwinger equation yields almost perfect overlap with the cavity eigenfrequency changes as calculated by COMSOL (orange and pink filled circles), which are based on the eigenvalues of the solutions. We attribute the small difference that is observed mostly to the way joined data sets are handled in COMSOL, which involves projection on an intermediate mesh. This is known to cause loss of information and introduces a small error when integrating radiation patterns.

### C. Subtracting fields

Figure 3a of the main paper shows the field profile $\mathbf{E}_\mathrm{p}$ of a cavity perturbed by an antenna on a glass substrate. To increase the visibility of the radiation pattern, that figure and Fig. S7 show the field amplitude for a cavity placed 0.3 $\mu$m from the substrate and antenna. To calculate the full cavity perturbation formula, it is necessary to find the unperturbed cavity field profile (Fig. S7a, $\mathbf{E}_0$) and subtract this from $\mathbf{E}_\mathrm{p}$ in order to obtain the field $\delta\mathbf{E}$ (Fig. S7b). The teal line surrounding the field profiles represents a perfectly matched layer (PML), which is used in all calculations discussed in this paper, while the dashed black line is the boundary which we used for the calculation of the surface integral of equation (1).

A pitfall in subtracting fields from different eigenfrequency simulations lies in the arbitrary choice of amplitude and phase of the solutions. To overcome this problem, we monitor the amplitude and phase in both simulations (with and without antenna) in a point where modification of the field profile due to the perturbing antenna is expected to be negligible. This can be, for example, a point in the field maximum of the cavity mode far away from the perturbation, thus allowing to correct for possible differences in amplitude and phase between the calculations. To obtain the data in Fig 3b, a single phase correction was performed, to match the phase at $\Delta_\mathrm{s} = -3$ to the unperturbed phase, in a mode maximum at large distance from the perturbing particle.

### IV. COUPLED MODE THEORY

We will describe the interactions between cavity and antenna using coupled mode theory [8], essentially modeling the system as coupled harmonic oscillators with Lorentzian response. We note that while it is possible to treat the antenna as a harmonic oscillator without making the Lorentzian approximation, all essential physics is captured in the simpler Lorentzian model. We treat the decay in a common (overlapping) radiation continuum, and its possible backaction on both antenna and cavity, by considering the 'environment' as a third mode coupled to both antenna and cavity as well as to an independent decay port. The complex mode amplitudes of cavity ($a$), antenna ($b$) and environment ($c$) are normalized such that their magnitude squared equals the energy in each degree of freedom. They
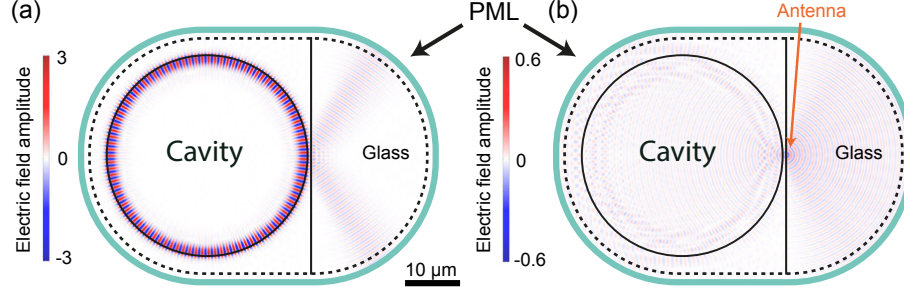
FIG. S7. **Simulated field profiles.** a) The simulated field profile $\mathbf{E}_0$ for a cavity in the absence of perturbing particles. b) The field profile $\delta\mathbf{E}$ of the perturbing antenna. This profile is obtained by subtracting the fields in (a) from those shown in Fig. 3a of the main paper. In both (a) and (b), the teal line surrounding the field profiles represents a perfectly matched layer (PML).

are collected in vector $\mathbf{a} = (a, b, c)^{\mathrm{T}}$. The equations of motion of the system (in absence of driving fields) can be written as

$$\frac{\mathrm{d}\mathbf{a}}{\mathrm{d}t} = (-\mathrm{i}\Omega - \Gamma)\,\mathbf{a}, \tag{S25}$$

where

$$\Omega = \begin{pmatrix} \omega_c & -\tilde{g}_c^* & -\tilde{g}_\kappa \\ -\tilde{g}_c & \omega_0 & -\tilde{g}_\gamma^* \\ -\tilde{g}_\kappa^* & -\tilde{g}_\gamma & \omega_e \end{pmatrix} \tag{S26}$$

is a Hermitian matrix containing the resonance frequencies and coupling rates. These coupling rates can in general be complex, and we will write them later as $\tilde{g}_j = g_j e^{\mathrm{i}\phi_j}$ with real $g_j$ and $\phi_j$. The matrix

$$\Gamma = \begin{pmatrix} \kappa_0/2 & 0 & 0 \\ 0 & \gamma_0/2 & 0 \\ 0 & 0 & \zeta/2 \end{pmatrix} \tag{S27}$$

is also Hermitian and contains the damping rates to the different independent coupling channels, which are associated with an individual mode $a$, $b$, and $c$. As such, the output fields $\mathbf{s} = (s_a, s_b, s_c)^{\mathrm{T}}$ in these ports can be written as $\mathbf{s} = K\mathbf{a}$, where

$$K = \begin{pmatrix} \sqrt{\kappa_0} & 0 & 0 \\ 0 & \sqrt{\gamma_0} & 0 \\ 0 & 0 & \sqrt{\zeta} \end{pmatrix}. \tag{S28}$$

These equations satisfy time reversal symmetry and conservation of energy, assured by the hermiticity of $\Omega$ and $\Gamma$ together with the condition $K^*K = 2\Gamma$. We now introduce the detunings $\Delta_c = \omega - \omega_c$, $\Delta = \omega_c - \omega_0$ and $\Delta_e = \omega_c - \omega_e$. The eigenmodes can be found by solving the system $M\mathbf{a} = \mathbf{0}$ where

$$M = I\omega - \Omega + \mathrm{i}\Gamma = \begin{pmatrix} \Delta_c + \mathrm{i}\kappa_0/2 & \tilde{g}_c^* & \tilde{g}_\kappa \\ \tilde{g}_c & \Delta_c + \Delta + \mathrm{i}\gamma_0/2 & \tilde{g}_\gamma^* \\ \tilde{g}_\kappa^* & \tilde{g}_\gamma & \Delta_c + \Delta_e + \mathrm{i}\zeta/2 \end{pmatrix}. \tag{S29}$$

Since we assume the cavity and antenna are weakly coupled and we are only interested in the perturbed cavity mode, we can neglect $\Delta_c$ in the second and third row of $M$. The solution is

$$\Delta_c = \frac{g_\kappa^2\left(\Delta + \mathrm{i}\frac{\gamma_0}{2}\right) + g_c^2\left(\Delta_e + \mathrm{i}\frac{\zeta}{2}\right) - 2g_c g_\kappa g_\gamma \cos\Phi}{\left(\Delta + \mathrm{i}\frac{\gamma_0}{2}\right)\left(\Delta_e + \mathrm{i}\frac{\zeta}{2}\right) - g_\gamma^2} - \mathrm{i}\kappa_0, \tag{S30}$$

where we have introduced $\Phi = \phi_c + \phi_\kappa + \phi_\gamma$.

It is instructive to consider the case where the cavity mode is absent ($a = 0, g_c = g_\kappa = 0$). In that case, the power radiated via the environment into port $s_c$ is equal to $\zeta g_\gamma^2 |b|^2/(\Delta_e^2 + \zeta^2/4)$. We therefore define the rate

$$\gamma_1 = \frac{\zeta g_\gamma^2}{\Delta_e^2 + \zeta^2/4}, \tag{S31}$$

which is the rate at which the antenna decays into the common radiation continuum if the cavity were not there. Likewise, we consider the case without the antenna ($b = 0, g_c = g_\gamma = 0$), and define

$$\kappa_1 = \frac{\zeta g_\kappa^2}{\Delta_e^2 + \zeta^2/4}, \tag{S32}$$

which is the rate at which the cavity would decay into this channel in absence of the antenna. In the latter case, the eigenmode would have detuning

$$\Delta_c^{(b=0)} = \frac{\Delta_e}{\zeta} \kappa_1 - i\frac{\kappa}{2}, \tag{S33}$$

where $\kappa = \kappa_0 + \kappa_1$ is the *total* decay rate of the cavity without the antenna. We now specifically write the general solution as $\Delta_c = \Delta_c^{(b=0)} + \delta\Delta_c$, such that $\delta\Delta_c$ is the *change* of the eigenmode frequency due to the presence of the antenna and $\delta\Delta_c = \delta\omega_c - i\delta\kappa/2$. Taking the limit of $\zeta$ to infinity, which effectively amounts to setting $\Delta_e = 0$, it reads

$$\delta\Delta_c = \frac{g_c^2 - \eta^2\kappa\gamma/4 + ig_c\eta\sqrt{\kappa\gamma}\cos\Phi}{\Delta + i\gamma/2}, \tag{S34}$$

where we have introduced $\eta = \sqrt{(\kappa_1\gamma_1)/(\kappa\gamma)}$; a number between 0 and 1 that is related to the overlap of the radiation of both modes. This is expression is equivalent to equation (3) in the main text.

Next, let us turn to the relation of this model to the phase difference $\delta\phi$ as it appears in the Bethe-Schwinger equation. To this end, we express the field in the environment $c$, compared to the field in the cavity $a$. Its full expression (still taking $\Delta_e = 0$) is

$$\frac{c}{a} = \frac{2ie^{-i\phi_\kappa}}{\zeta} \frac{g_\kappa\left(\Delta + i\frac{\gamma_0}{2}\right) - g_c g_\gamma e^{i\Phi}}{\Delta + i\frac{\gamma}{2}} \tag{S35}$$

The phase $\delta\phi$ must be equal to the phase difference of the above in absence of the particle ($g_c = g_\gamma = 0$) and its phase in absence of direct coupling between cavity and environment ($g_\kappa = 0$). Performing this subtraction yields

$$\delta\phi = \pi + \Phi - \arg\left(\Delta + i\frac{\gamma}{2}\right), \tag{S36}$$

showing that the phase difference of the two decay paths is directly related to the (relative) phases of the coupling rates via $\Phi$ and the phase response of the antenna [9]. It becomes clear that the standard case, where the two paths interfere destructively on resonance ($\Delta = 0$), occurs for $\Phi = \pi/2$, such that $\delta\phi = \pi$.

Finally, we note that it is straightforward to eliminate the environment mode $c$ from the model to construct an equivalent system of equations $M'(a, b)^{\mathrm{T}} = \mathbf{0}$. In that case the total damping rates $\kappa$ and $\gamma$ of the uncoupled cavity and antenna appear on the diagonal:

$$M' = \begin{pmatrix} \Delta_c + i\frac{\kappa}{2} & e^{-i\phi_c}\left(g_c + \frac{i}{2}\sqrt{\kappa_1\gamma_1}e^{i\Phi}\right) \\ e^{i\phi_c}\left(g_c + \frac{i}{2}\sqrt{\kappa_1\gamma_1}e^{-i\Phi}\right) & \Delta + i\frac{\gamma}{2} \end{pmatrix}. \tag{S37}$$

We can choose the phase $\phi_c = 0$ without loss of generality, such that

$$M' = \begin{pmatrix} \Delta_c + i\frac{\kappa}{2} & g_c + \frac{i}{2}\sqrt{\kappa_1\gamma_1}e^{i\Phi} \\ g_c + \frac{i}{2}\sqrt{\kappa_1\gamma_1}e^{-i\Phi} & \Delta + i\frac{\gamma}{2} \end{pmatrix}. \tag{S38}$$

Note that the off-diagonal matrix elements of $M'$, representing coupling between cavity and antenna, are now no longer Hermitian.
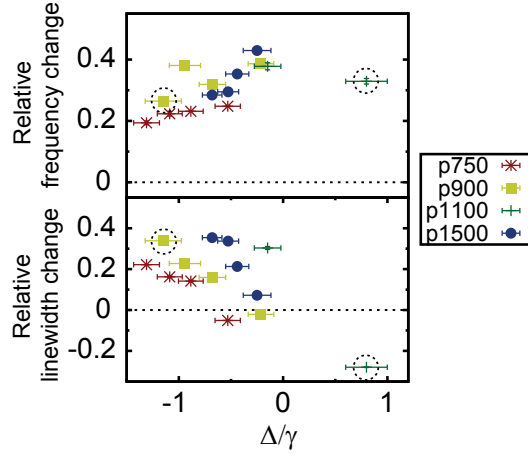
FIG. S8. **Varying the antenna array pitch.** Changing the pitch along the antenna short axis (between 750 and 1500 nm) does not greatly affect the cavity eigenfrequency shift. For all arrays, we observe cavity blueshifts (top panel) and linewidth narrowing (bottom panel). Note that in the bottom panel, the different pitches cross the point of zero linewidth change at slightly different values of $\Delta/\gamma$. Modification of the single particle polarizability due to the array is the most likely cause of this behaviour. The values on the vertical axis are corrected for the unit-cell area and the points which are surrounded by a dashed circle correspond to the arrays used to generate Fig. 2a of the main text. Errors on the mean (vertical axis) fall mostly within the plot markers and the error on the horizontal axis is one standard deviation, retrieved from a Gaussian fit to the sum of squared residuals (obtained by displacing the fit result). Due to limited detector range, a reliable horizontal error for the data at P1100,$\Delta/\gamma \approx 0.8$ could not be obtained using this method. The error on this data point was thus set equal to the error for array P1100,$\Delta/\gamma \approx -0.15$.

## V. VARYING ANTENNA PITCH

The text of the main paper shows the results and analysis of antenna arrays with pitch 800(1500) nm along the long(short) axis of the antennas. More pitches are, however, experimentally investigated and Fig. S8 shows the main results which we obtain when varying the pitch along the short axis (750-1500 nm) of the antennas, while the pitch along the antenna long axis is kept constant at 800 nm. In this figure, the points which are surrounded by a dashed circle correspond to the arrays used to generate Fig. 2a of the main text. The main conclusion that can be drawn from Fig. S8 is that, qualitatively, the different arrays behave the same: all arrays induce blueshifts of the cavity resonance frequency (top panel) and linewidth narrowing (bottom panel) of the cavity on approaching $\Delta/\gamma = 0$. With changing pitch, the value of $\Delta/\gamma$ where the "relative linewidth change" equals 0, slightly varies. We attribute this effect to the influence of the array on the single particle polarizability. Remarkably, for the largest possible detuning we measure linewidth narrowing up to 30% for a pitch of 1100 nm.

As in the main paper, the values of $\Delta/\gamma$ are retrieved from a fit of the normal-incidence transmission spectra using a Lorentzian lineshape. Lattice sum calculations [10] are performed to exclude strong modification of $\Delta$ due to the change of effective angle of incidence (in the experiment) with respect to the normal-incidence transmission spectra. In addition, total internal reflection measurements on the samples with a 1500 nm pitch showed no significant change of $\Delta$ with respect to the values obtained from the normal-incidence measurements.

---

[1] R. A. Waldron, Proc. IEE Part C Monogr. **107**, 272 (1960).
[2] H. A. Bethe and J. Schwinger, *Perturbation theory for cavities* (Massachusetts Institute of Technology, Radiation Laboratory, Cambridge, 1943).
[3] Due to the different (engineering) convention used in COMSOL, implementation of this formula requires to switch the sign in front of the surface integral from (-) to (+).
[4] D. K. Armani, T. J. Kippenberg, S. M. Spillane, and K. J. Vahala, Nature **421**, 925 (2003).
[5] G. Anetsberger, O. Arcizet, Q. P. Unterreithmeier, R. Rivière, A. Schliesser, E. M. Weig, J. P. Kotthaus, and T. J. Kippenberg, Nat. Phys. **5**, 909 (2009).
[6] L. Novotny and B. Hecht, *Principles of Nano-Optics* (Cambridge University Press, Cambridge, 2012).
[7] COMSOL personal communication.
[8] W. Suh, Z. Wang, and S. Fan, IEEE J. Quant. Electron. **40**, 1511 (2004).

[9] Due to the different (engineering) convention used in COMSOL, implementation of this formula requires to place a (-) sign in front of the right-hand side of expression (S36) when analyzing COMSOL data.

[10] F. J. García de Abajo, Rev. Mod. Phys. **79**, 1267 (2007).